RESEARCH ARTICLE

ADVANCED ENGINEERING MATERIALS
www.aem-journal.com

Check for updates

Overview of Ruthenium Thin Films Annealed by Microsecond Scanning UV Pulsed Laser: Structural, Electrical, and Failure Modes Analysis

Richard Daubriac, Leonardo Cancellara, Zeinab Chehadi, Lu Lu, Louis Thuries, Mohamed Ali Khaled, Fabien Roze, Nicolas Jourdan, Zsolt Tokei, Armel Descamps-Mandine, Teresa Hungria, Pier-Francesco Fazzini, Toshiyuki Tabata, and Karim Huet*

Ruthenium (Ru) has been identified as a durable and relevant substitute to copper (Cu) to answer the access resistance lowering of the back-end-of-line (BEOL) metal levels, which is a high-priority concern for future devices. Herein, the nonequilibrium and local properties of pulsed scanning laser annealing (SLA) technique are used to enhance the structural and electrical properties of thin polycrystalline Ru layers (<30 nm). For the best annealing conditions, transmission electron microscopy observations show a substantial grain size enlargement, with large grains (≈80 nm) occupying the whole layer height. It goes with a 53% resistivity reduction, measured by 4-point probe, confirming the strong grain boundary scattering reduction. A Mayadas–Shatzkes model incorporating temperature-dependent resistivity measurements allows the extraction of promising reflectivity and specularity coefficients of around 0.58 and 0.98, respectively. Beyond the best conditions, failure modes for devices integration are observed, such as surface wrinkling and local buckling. Given the studied system, a semiquantitative analysis of these phenomena is given and simulations based on the finite element method are used to find further optimal annealing conditions. This study confirms the potential of Ru as a promising BEOL material, but also SLA as a convincing technique for future 3D architectures.

1. Introduction

The extreme downscaling and versatility of metal-oxide-semiconductor architectures for future technology nodes require new materials and processes to enable the improvement of devices performances and the reduction of their energy consumption. One of these challenges is related to the size reduction of the current copper (Cu)-made back-end-of-line (BEOL) metallic interconnections, both top and bottom levels (M1–M10). Indeed, the electron mean free path (e-MFP) of this material (≈40 nm) is in the same order of magnitude as interconnects dimensions (M1–M3), arising inevitable surface scattering (SS) contributions. Among other attractive materials, Ru has been identified as a promising alternative for scalability to Cu, thanks to its short e-MFP (<7 nm), low resistivity (7.6 μΩ cm), and good electromigration properties (5.0 MA cm^{-2}, 1000 h at 300 °C). In addition to new materials, innovative processes are required.[1–6] Moreover, thanks to its high fusion temperature (2334 °C), Ru allows a wider process window than Cu (1085 °C) for the investigation of out-of-equilibrium and innovative thermal treatments such as laser

R. Daubriac, L. Cancellara, M. A. Khaled
Laboratoire d'Analyse et d'Architecture des Systèmes (LAAS)
CNRS
Université de Toulouse
31400 Toulouse, France
E-mail: richard.daubriac@wanadoo.fr

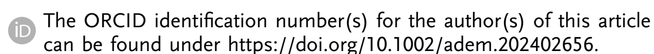
The ORCID identification number(s) for the author(s) of this article can be found under https://doi.org/10.1002/adem.202402656.

© 2024 The Author(s). Advanced Engineering Materials published by Wiley-VCH GmbH. This is an open access article under the terms of the Creative Commons Attribution-NonCommercial License, which permits use, distribution and reproduction in any medium, provided the original work is properly cited and is not used for commercial purposes.

DOI: 10.1002/adem.202402656

Z. Chehadi, L. Lu, L. Thuries, F. Roze, T. Tabata
Laser Systems & Solutions of Europe (LASSE)
SCREEN Semiconductor Solutions Co., Ltd.
145 Rue des Caboeufs Bâtiment D, 92230 Gennevilliers, France

N. Jourdan, Z. Tokei
Institut de MicroElectronique et Composants (IMEC)
Kapeldreef 75, B-3001 Leuven, Belgium

A. Descamps-Mandine, T. Hungria
Centre de MicroCaractérisation Raimond Castaing
3 Rue Caroline Aigle, 31400 Toulouse, France

annealing.[7–10] Pulsed laser annealing is one of the best candidates to succeed or supplement conventional annealing techniques as it allows achieving local (≈100 nm from surface), ultrafast (micro-to-nanosecond), and significant (up to 2000 °C) thermal budgets. In this work, we report on the unique structural, electrical, mechanical properties, and failure modes emerging from the interaction between the microsecond UV pulsed scanning laser annealing (SLA) and Ru material. For this study, 30 nm thick Ru layers on top of TiN(1.5 nm)/SiO_2(100 nm)/Si were irradiated using a SCREEN platform equipped with a monochromatic (between 300 and 400 nm) microsecond scanning UV pulsed laser. A large range of thermal budgets was applied by fixing the energy density (ED) and varying the irradiation time (IT) to capture the different dynamics of the laser process.

The first part of this article is dedicated to the structural analysis of the nonannealed and annealed layers, with a focus on the conformity of the stack, the grain size distribution evolution, and the phases present inside the films, using transmission electron microscopy (TEM). In the second part, we present the electrical results measured by 4-point probe (4PP) method depending on the applied laser conditions along with calculation models to quantify the grain boundary and SS phenomena inside our Ru layers. In the third part, we discuss the observed failure modes at different dimension scales: the wrinkles (micrometer scale) and the buckling (nanometer scale) phenomena. A fourth part is dedicated to the simulation of the laser process to corroborate our experiments results and to determine optimized laser conditions for future designs of experiments. The final part of the paper is devoted to the global perspectives arising out of our study, from the Ru material and laser annealing points of view.

2. Experimental Results and Discussion

2.1. Structural Study

A combination of high-resolution TEM (HR-TEM) and scanning TEM (STEM)–high-angle annular dark field (HAADF)/bright field (BF) measurements modes was used on three laser-annealed samples (10 µs (A), 20 µs (B), and 40 µs (C) at 15.0 mJ cm^{-2}) along with the reference layer (Ref) to observe the impact of the laser annealing on the layer stack integrity, the grain shape evolution, and measure the thickness consistency.

For all the selected conditions, no diffusion of Ru into the SiO_2 buried oxide was observed (**Figure 1**a). This means that the diffusion barrier property of the TiN interlayer is not altered by the high temperatures and fast variations experienced during the laser annealing process. Energy-dispersive X-ray spectroscopy (EDX) analysis performed on the same samples corroborates this result (Figure S1 and S2, Supporting Information). The average thickness of the Ru layers has been evaluated around $t_{Ru} = 31.90 \pm 0.50$ nm, confirming the good uniformity of the deposition process across the 300 mm wafer. Moreover, a low surface and interface roughness was observed by TEM. Atomic force microscopy (AFM) measurements confirmed this surface flatness with a calculated R_q lower than 0.7 nm (Figure S3, Supporting Information). Moreover, a clear increase in the grain size is evidenced: starting from grains smaller than the film thickness ($r < t_{Ru}$) with randomly oriented boundaries (Ref and sample A), to column-shaped large grains, widened by the SLA up to the film thickness ($r \geq t_{Ru}$), with perpendicular grain boundaries (indicated by the white dotted line, samples B and C) (Figure 1b). Grazing incidence X-ray diffraction (GIXRD) (1° grazing angle) measurements (Figure S4, Supporting Information) showed that hexagonal Ru is the dominant crystal structure, with a preferential out-of-plane orientation along the Ru(0001).[11–13] The plan-view TEM images presented in **Figure 2**a show a significant increase in the grain size when increasing the IT. Moiré patterns can be observed in the images of the Ref and A samples, with some of them persisting in the sample B images. In our system, this contrast effect characterizes the superposition of slightly misoriented grains whose sizes are inferior to the layer thickness, thus validating the previous conclusions based on cross-sectional observations (Figure 2b).

In order to avoid the impact of such effect on the extraction of the average grain size, we opted for the polygon method. It consists in manually circling the borders of the grains and calculating the areas of the so-drawn polygons. From the extracted areas and by approximating the shape of the grains to circles, we can deduce values of the effective grain diameter d_{eff}. The relative grain size distributions of the four selected conditions are presented in Figure 2a. For each dataset, Gaussian and lognormal fits were applied to evaluate their respective type of distributions and their parameters. Ref and A samples exhibit similar Gaussian distributions with low standard deviations, describing layers with homogeneously distributed and superimposed small grains of around 15 nm. For samples B and C, lognormal distributions with large standard deviations are inferred from the fits, evidencing a wide range of grain sizes. When increasing the thermal budget, the minimum and maximum values of these distributions shift toward larger values and progressively spread out: 20–70 nm for sample B and 30–140 nm for sample C, respectively. As emphasized by these results, the grain growth (GG) does not come from the simultaneous merging of the initial grains to obtain a few numbers of homogeneously distributed large grains but originates from a partial grain coalescence that leads to very large grains to the detriment of some small grains. The evolution of the mean grain size as a function of the IT is plotted in Figure 2b, along with their respective standard deviation values. A red-dotted guideline depicting the well-known growth saturation phenomenon[14,15] has been superposed to the data points in addition to the variations of minima and maxima (red area). Moreover, gray dotted straight lines are added to distinguish properly the asymptotic behaviors. Their intersections at ≈10 and ≈23 µs are annotated IT(r_1) and IT(r_2), respectively. From this graph, we can assume the existence of three different regimes. In the first regime (0 to IT(r_1)), the thermal budget is too low to involve a significant enlargement of the

P.-F. Fazzini
Laboratoire de Physique et Chimie des Nano-Objets (LPCNO)
INSA
CNRS
Université de Toulouse
7 avenue du Colonel Roche, 31400 Toulouse, France

K. Huet
SCREEN SPE Germany GmbH
SCREEN Semiconductor Solutions, Co. Ltd.
Fraunhoferstraße 7, 85737 Ismaning, Germany

© 2024 The Author(s). Advanced Engineering Materials published by Wiley-VCH GmbH

15272648, 2025, 4, Downloaded from https://advanced.onlinelibrary.wiley.com/doi/10.1002/adem.202402656, Wiley Online Library on [05/02/2026]. See the Terms and Conditions (https://onlinelibrary.wiley.com/terms-and-conditions) on Wiley Online Library for rules of use; OA articles are governed by the applicable Creative Commons License

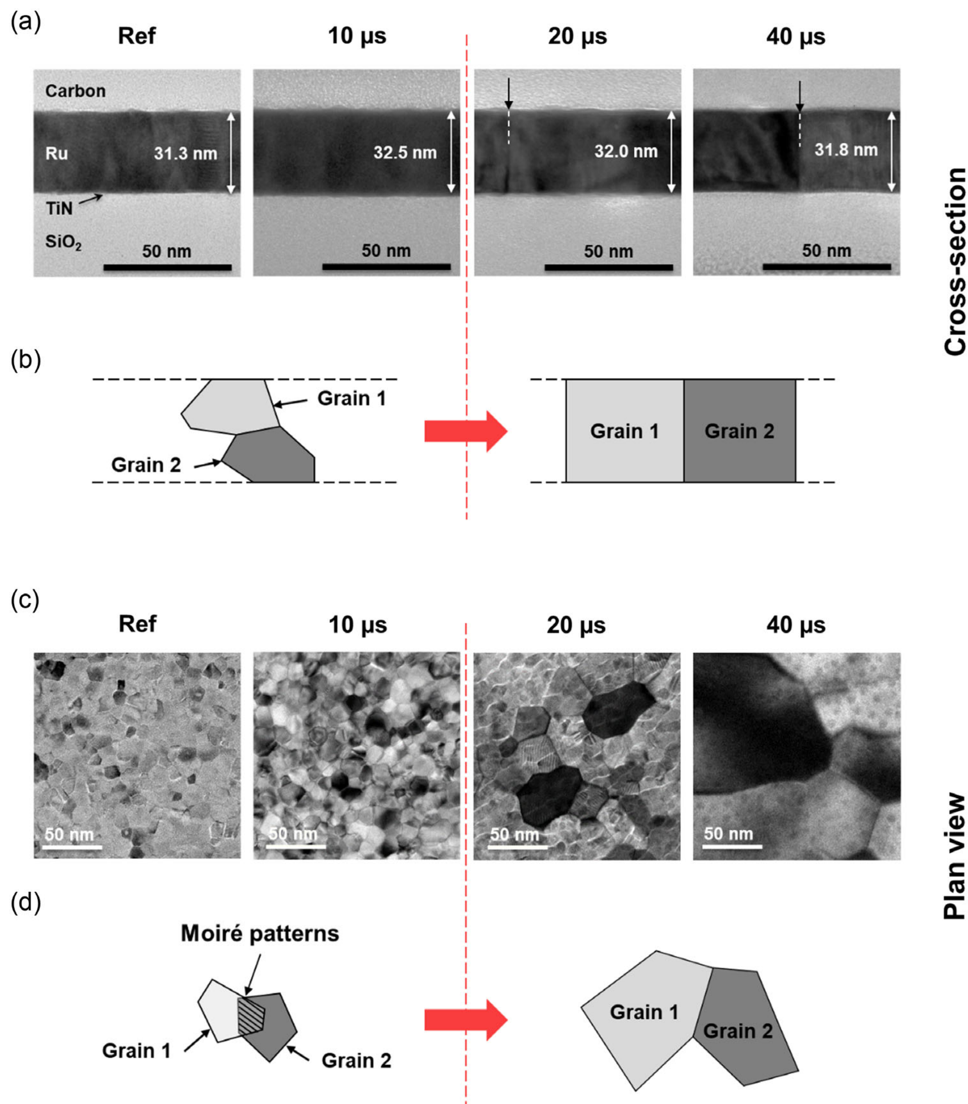

Figure 1. Cross-sectional a) and plan view c) TEM images made on as-deposited (Ref) and laser-annealed films at 15.0 mJ cm^{-2} with different IT (10 µs (A), 20 µs (B) and 40 µs (C)). b,d) Associated schematics of the structural changes when applying laser annealing.

grains (an increase of around ≈1.7 nm) and the curve stays stable. Between 10 (IT(r_1)) and 30 (IT(r_2)) µs, the energy transmitted by the laser is higher than the activation energy required to trigger the GG and a linear grain size increase is observed (from 12 to 82 nm; in average). Finally, from 30 µs, the internal stress inside the layer is strengthened by the grain size enlargement, which prevents the phenomenon itself from continuing (see Section 2.3). It is shown by the asymptotic behavior around ≈90 nm. Thanks to the SLA, we were able to obtain a thin Ru layer with grains filling completely the layer thickness (30 nm) and extending laterally up to 140 nm. For ITs longer than 20 µs, the grain size values are sufficiently higher than the Ru e-MPF (<7 nm) to exclude conductivity deterioration rising from structural dimensions.

2.2. Electrical Study

2.2.1. 4PP Versus IT—Laser Regimes Identification

4PP measurements have been performed on the reference layer and several areas irradiated by SLA at 15.0 mJ cm^{-2} with different IT ranging between 1.3 and 40 µs. From the measured sheet resistance R_S we can directly calculate the resistivity $\rho = R_S \times t_{Ru}$, as the thickness of the layer remains constant after the laser annealing process (t_{Ru} is approximated to 30 nm). The resulting resistivity as function of the IT is presented in **Figure 3**. The resistivity of the as-deposited layer (0 µs) is 22.5 µΩ cm ($R_S = 7.5\ \Omega\ sq^{-1}$), which is close to the lowest thermal budget (15.0 mJ cm^{-2}, 1.3 µs).

© 2024 The Author(s). Advanced Engineering Materials published by Wiley-VCH GmbH

15272648, 2025, 4, Downloaded from https://advanced.onlinelibrary.wiley.com/doi/10.1002/adem.202402656, Wiley Online Library on [05/02/2026]. See the Terms and Conditions (https://onlinelibrary.wiley.com/terms-and-conditions) on Wiley Online Library for rules of use; OA articles are governed by the applicable Creative Commons License

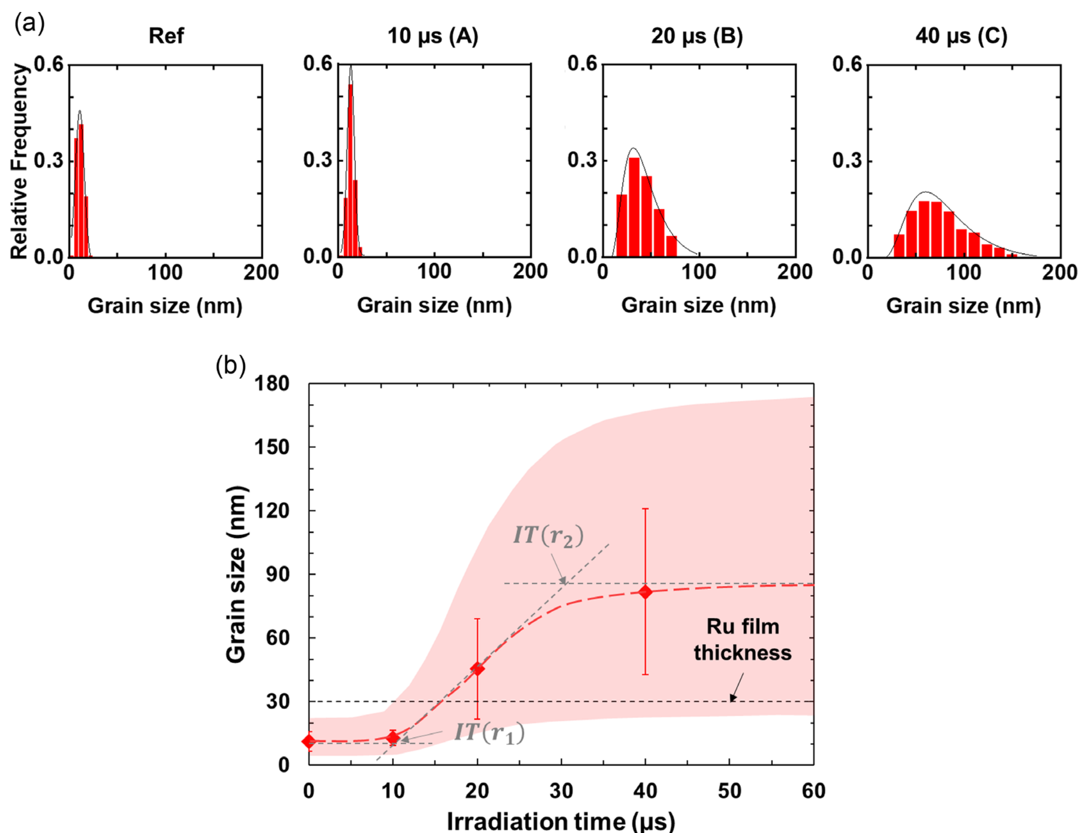

Figure 2. a) Grain size distribution histograms plotted in relative frequency for the as-deposited (Ref) and laser-annealed films at 15.0 mJ cm^{-2} with different IT (10 µs (A), 20 µs (B), and 40 µs (C)). The grain sizes were determined thanks to the polygon method. b) Evolution of the average grain size as function of the IT. The error bars correspond to the standard deviations. A red dotted guideline is added to depict the well-known growth saturation phenomenon[14,15] and a red area to illustrate the variations of the minimum and maximum values of the grain size. Gray dotted straight lines are superimposed on the red guideline to highlight the asymptotic behaviors. Their intersections are annotated IT(r_1) and IT(r_2).

Between the reference value and that of to the highest thermal budget (15.0 mJ cm^{-2}, 40 µs), three different regimes are noticeable (highlighted with asymptotic dotted lines in Figure 3). In the first regime (0–5 µs), the impact of the laser annealing process on the resistivity is very low (<4% reduction). Then, in the second regime (5–23 µs), the resistivity decreases linearly when increasing the IT (up to ≈50% resistivity reduction). Finally, in the third regime (23–40 µs), the resistivity reaches a plateau around $\rho_{min}(300\ K) = 10.4\ \mu\Omega\ cm$ (≈53% resistivity reduction). The two transition points between these three regimes are evaluated around 5 and 23 µs IT, annotated IT(ρ_1) and IT(ρ_2) in Figure 3, respectively. In comparison with the grain size evolution shown in Figure 3b, the transition point IT(ρ_1) is shifted by 5 µs toward the lower IT values in comparison with IT(r_1). Similarly, a gap of 7 µs is observed between IT(ρ_2) and IT(r_2). This means that the linear decrease of the resistivity, defined as the second regime, is reached even though the average grain size has enlarged by a few nanometers. As an example, comparing the reference and sample A, increasing the average grain size by 1.7 nm improves the resistivity by 17% (22.5 µΩ cm for the reference and 18.8 µΩ cm at 10 µs) (Figure 3, inset). Moreover, interestingly, the significant increase in grain size measured between samples B and C (from 45.4 to 81.9 nm) involves a 3% improvement of the reference's resistivity (from 12.4 to 10.4 µΩ cm). However, even if this last optimization between these two samples appears minor, it is actually the most substantial step to reach the lowest possible resistivity values in the third regime (≈15% resistivity reduction from sample B to C). Thereby, with this analysis, we evidenced that a slight offset exists between the resistivity and grain size evolution with the IT. This specific point is extensively studied in one of the following sections devoted to resistivity versus grain size modeling through the Mayadas–Shatzkes (MS) theory.

2.2.2. 4PP Versus Temperature—Electron–Phonon Coupling

In Figure 1b, 2, we showed that our samples present substantial difference in their grain size distribution. 4PP measurements as a function of the temperature have been performed on the four samples down to around 20 K to evaluate the impact of such distinct grain size distributions on the fundamental electrical properties of Ru. The obtained curves presented in **Figure 4**a exhibit the characteristic trend of electrical transport dominated by electron–phonon scattering.[16–21] This behavior is well described by the following Bloch–Gruneisen (BG) model for metals (Equation (1)):

 © 2024 The Author(s). Advanced Engineering Materials published by Wiley-VCH GmbH

15272648, 2025, 4, Downloaded from https://advanced.onlinelibrary.wiley.com/doi/10.1002/adem.202402656, Wiley Online Library on [05/02/2026]. See the Terms and Conditions (https://onlinelibrary.wiley.com/terms-and-conditions) on Wiley Online Library for rules of use; OA articles are governed by the applicable Creative Commons License

15272648, 2025, 4, Downloaded from https://advanced.onlinelibrary.wiley.com/doi/10.1002/adem.202402656, Wiley Online Library on [05/02/2026]. See the Terms and Conditions (https://onlinelibrary.wiley.com/terms-and-conditions) on Wiley Online Library for rules of use; OA articles are governed by the applicable Creative Commons License

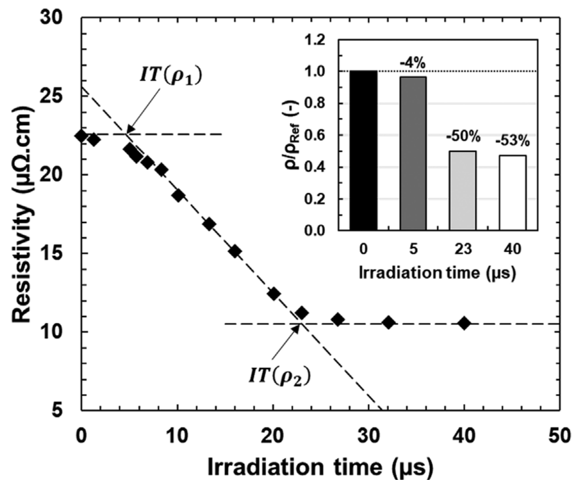

Figure 3. Resistivity as a function of the IT for 30 nm thick Ru layers annealed by SLA at 15.0 mJ cm^{-2} with different IT ranging between 1.3 and 40 µs. The resistivity of the as-deposited layer is added to the graph at IT = 0 µs (22.5 µΩ cm). The asymptotic dotted guidelines illustrate the three different regimes of the resistivity curve and IT(ρ_1) and IT(ρ_2), their intersection points. (Inset) Histogram graph comparing the resistivity values of the reference layer (0 µs) with samples annealed at different IT of 5, 23, and 40 µs (C) at an ED of 15.0 mJ cm^{-2}.

$$\rho_{\text{total}}(T) = \rho_{\text{para}} + \Re(\Theta_{\text{D}}) \times \left(\frac{T}{\Theta_{\text{D}}}\right)^5 \times \int_0^{\Theta_{\text{D}}/T} \frac{x^5}{(e^x - 1)(1 - e^{-x})} \text{d}x \tag{1}$$

with the parasitic resistivity ρ_{para}, the Debye temperature Θ_{D}, and the BG prefactor $\Re(\Theta_{\text{D}})$, distinctive of the electron–phonon coupling. Assuming an average Debye temperature of $\Theta_{\text{D}} = 415$ K,[22–24] $\Re(\Theta_{\text{D}})$ and ρ_{para} have been estimated by using a 2-variable fitting procedure. Figure 4b displays both parameters fit results as a function of the grain size. The electron–phonon coupling factor increases when the grain sizes increase, which is consistent with a growing interaction between electrons and the crystal lattice as the grains are enlarging. The trend of this parameter suggests an asymptotic behavior to a maximum value corresponding to the bulk monocrystalline Ru material. For the parasitic resistivity, a comparable trend is observable, except it involves decreasing values to a minimum that should be close to 0 when approaching 0 K. This is consistent with the progressive reduction of the grain boundary contribution to the resistivity. Similar to the study of the structural properties, a clear distinction between small grains (reference and A) and large grains (B and C) can be noticed for both fitted parameters. The bulk temperature-dependent resistivity $\rho_{\text{B}}(T)$ curve has been modeled assuming a room temperature (RT) resistivity of $\rho_i = 7.60$ µΩ cm,[25–28] no parasitic resistivity ($\rho_{\text{para}} = 0$ µΩ cm), and an electron–phonon coupling of $\Re(\Theta_{\text{D}}) = 51$ µΩ cm (Figure 4a). To follow these criteria, a Debye temperature of 445 K was required, which implies $\Theta_{\text{D}_{\text{bulk}}} > \Theta_{\text{D}_{\text{film}}} = 415$ K. This can be explained by the observed phonon-softening phenomenon that has been described in many studies for several metals.[17,19–21,26,29] These values should not be taken as absolute values as we arbitrarily set $\Theta_{\text{D}_{\text{film}}}$ at 415 K (based on an average of values found in literature). However, fixing another value of $\Theta_{\text{D}_{\text{film}}}$ does not change the obtained relation: $\Theta_{\text{D}_{\text{bulk}}} > \Theta_{\text{D}_{\text{film}}}$.

2.2.3. 4PP Versus Grain Size—Reflectivity and Specularity Coefficients Determination

In polycrystalline metallic layers, the two dominant and encountered scattering phenomena are the grain boundary scattering and the SS. Both are, respectively, well described by MS[30] and Fuchs–Sondheimer (FS)[31,32] models, which depict the resistivity variations as a function of the grain size and the layer

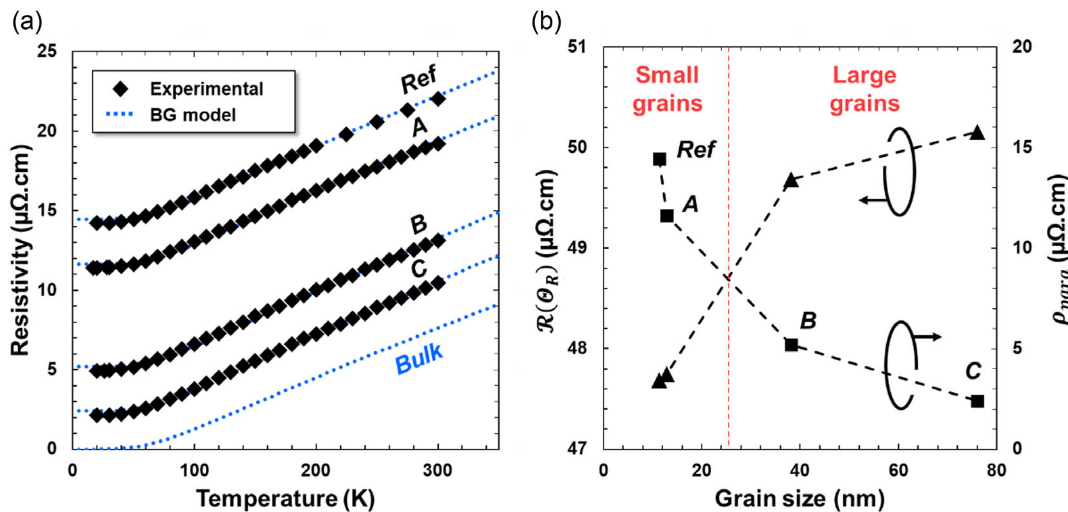

Figure 4. a) Measured resistivity as a function of the temperature for samples A, B, and C along with the reference layer (black diamonds). The four experimental curves have been fitted using the BG model (blue dotted lines). b) Corresponding electron–phonon coupling factor $\Re(\Theta_{\text{D}})$ and parasitic resistivity ρ_{para} found using the BG model, plotted as a function of their respective average grain size. Similar to the structural study, a clear distinction between small grains (reference and A) and large grains (B and C) can be noticed for both fitted parameters (red dotted line).

 © 2024 The Author(s). Advanced Engineering Materials published by Wiley-VCH GmbH

thickness. From these models, it is possible to extract two characteristic coefficients: the grain reflectivity R and the surface specularity p (Equation (2) and (3)).

$$\rho_{\mathrm{MS}} = \rho_i \left[1 - \frac{3}{2}\alpha + 3\alpha^2 - 3\alpha^3 \ln\left(1 + \frac{1}{\alpha}\right)\right]^{-1} \tag{2}$$

with

$$\alpha = \left(\frac{\lambda}{g}\right)\left(\frac{R}{1-R}\right)$$

and

$$\rho_{\mathrm{FS}} = \rho_i \left[1 - \left(\frac{3}{2k}\right)(1-p)\int_1^{\infty}\left(\frac{1}{t^3} - \frac{1}{t^5}\right)\left(\frac{1-e^{-\mathrm{kt}}}{1-pe^{-\mathrm{kt}}}\right)\mathrm{d}t\right]^{-1} \tag{3}$$

with

$$k = \frac{h}{\lambda}$$

To achieve a proper coefficient extraction, the MS model requires samples with a fixed layer thickness and varying grain sizes (resistivity versus grain size) while the FS model requires samples with a fixed grain size and different layers thicknesses (resistivity versus thickness). Also, in each of these conditions, both models can be combined to extract simultaneously R and p. As our study is constrained to a single thickness value (30 nm), the FS model cannot be used alone. However, it is appropriate to apply the MS model and the combined model MS + FS, using Equation (4).[33] Both MS and MS + FS models were applied to our set of data R and p in the 20–300 K range of temperatures and their results are discussed in the section below.

$$\rho_{\mathrm{total}} = \Delta\rho_{\mathrm{MS}} + \Delta\rho_{\mathrm{FS}} + \rho_i \tag{4}$$

with

$$\Delta\rho_{\mathrm{MS}} = \rho_{\mathrm{MS}} - \rho_i$$

$$\Delta\rho_{\mathrm{FS}} = \rho_{\mathrm{FS}} - \rho_i$$

As in most theoretical models, the number of fitting parameters can be arbitrarily large. In order to discuss consistently the obtained results, we used only one (R) for the MS model alone and two (R,p) for the MS + FS model. Besides these fitted variables, the initial resistivity ρ_i and the electron mean-free path λ are fixed parameters whose values depend on the temperature. For both constants, their temperature dependency was evaluated based on the 4PP versus temperature measurements presented in the previous section (Figure 4a). For the initial resistivity, we used four different $\rho_i(T)$ curves (plotted in Figure S5a, Supporting Information, calculation method presented in Supplementary Note S1): the modeled bulk resistivity $\rho_{\mathrm{B}}(T)$, two 30 nm thick film resistivities $\rho_{\mathrm{F1}}(T)$ and $\rho_{\mathrm{F2}}(T)$, and the experimental resistivity $\rho_{\mathrm{C}}(T)$ of sample C. At 300 K, their respective resistivities are: $\rho_{\mathrm{B}}(300\ \mathrm{K}) = 7.60\ \mu\Omega\ \mathrm{cm}$, $\rho_{\mathrm{F1}}(300\ \mathrm{K}) = 8.30\ \mu\Omega\ \mathrm{cm}$, $\rho_{\mathrm{F2}}(300\ \mathrm{K}) = 9.20\ \mu\Omega\ \mathrm{cm}$, and $\rho_{\mathrm{C}}(300\ \mathrm{K}) = 10.4\ \mu\Omega\ \mathrm{cm}$.[3,26–29] For the e-MFP, as our layers are mainly composed of (0001)-oriented hexagonal Ru (space group $P6_3/mmc$) (GIXRD, Figure S4, Supporting Information), the bulk value is expected to be $\lambda_{\mathrm{B}}(300\ \mathrm{K}) = 6.59\ \mathrm{nm}$[28] (giving a total product $\rho_{\mathrm{B}} \times \lambda_{\mathrm{B}} = 5.01 \times 10^{-16}\ \Omega\ \mathrm{m}^2$). Multiple $\lambda(T)$ curves were calculated considering three cases: 1) the absence of SS, 2) the presence of SS in the whole range of temperature, and 3) a mix between (1) and (2) depending on the e-MFP value in comparison with the layer thickness. Based on several studies,[34] the whole methodology to obtain each $\lambda_i(T)$ is detailed in Supplementary Note S2 and their associated curves are presented in Figure S6, Supporting Information. In addition to the R and p coefficient, we calculate the Bayesian information criterion (BIC) to compare rigorously our different theoretical models, each applied in the three cited cases.[35–37]

All the obtained R, p, and BIC values between 20 and 300 K are summarized in **Figure 5**a. Looking at $\mathrm{MS}(\lambda_{\mathrm{F1,F2}})$ and $\mathrm{MS+FS}(\lambda_{\mathrm{F1,F2}})$ models, we can observe that the SS phenomenon has a very small impact on the R, p and BIC results. Indeed, considering the e-MFP values compared to the film thickness (30 nm) and the measured surface roughness being lower than 0.7 nm (Figure S3, Supporting Information), one would expect that the SS phenomenon should have a negligible impact on the electrical properties. For these reasons, only the results involving no SS (i) are considered in the following discussion. In this particular case, we can see that $\mathrm{MS}(\lambda_{\mathrm{B}})$ and $\mathrm{MS+FS}(\lambda_{\mathrm{B}})$ models provide widely distributed R values and high BIC values, for all considered initial resistivities $\rho i(T)$. Similarly, for the $\mathrm{MS}(\lambda_{\mathrm{F1,F2}})$ and $\mathrm{MS+FS}(\lambda_{\mathrm{F1,F2}})$ models, either widely distributed R values or high BIC values are obtained when using initial resistivities $\rho_{\mathrm{B}}(T)$ and $\rho_{\mathrm{C}}(T)$. Consequently, this leaves $\mathrm{MS}(\lambda_{\mathrm{F1,F2}})$ and $\mathrm{MS+FS}(\lambda_{\mathrm{F1,F2}})$ models without SS and initial resistivities $\rho_{\mathrm{F1}}(T)$ and $\rho_{\mathrm{F2}}(T)$ as the most reliable models. All together, they give an average reflectivity coefficient $R \approx 0.64$ and specularity coefficient $p \approx 0.5$. However, it can be observed that the initial resistivity $\rho_i(T)$ has a significant impact on the final results. To evaluate this impact, additional fitting procedures have been performed on $\mathrm{MS}(\lambda_{\mathrm{B,F1,F2}})$ and $\mathrm{MS+FS}(\lambda_{\mathrm{B,F1,F2}})$ models without SS, by using a larger number of temperature-resistivity curves $\rho_i(T)$. They were selected identical to $\rho_{\mathrm{B}}(T)$ and $\rho_{\mathrm{C}}(T)$, but with $\rho_{\mathrm{B,C}}$ (300 K) comprised between 8.4 and 10.8 μΩ.cm (Figure S5b, Supporting Information). Thanks to this analysis (Figure S7, Supporting Information), we show that the $\mathrm{MS}(\lambda_{\mathrm{B}})$ and $\mathrm{MS+FS}(\lambda_{\mathrm{B}})$ models give large distributions of R for almost all $\rho_i(T)$. The only exceptions are for $\rho_{\mathrm{C}}(300\ \mathrm{K}) = 8.4\ \mu\Omega.\mathrm{cm}$, but the associated BIC values are high or the specularity coefficient $p \approx 0$, which is incompatible with the "no SS" case (i). To determine the ideal conditions, two criteria were defined: $\rho_i(T)$ curves giving specularity coefficients $p > 0.5$ (compatible with no SS, blue background in Figure S7, Supporting Information) and $\rho_i(300\ \mathrm{K}) < 10.4\ \mu\Omega.\mathrm{cm}$ (minimum experimental value, red dotted line in Figure S7, Supporting Information). For both $\mathrm{MS}(\lambda_{\mathrm{F1,2}})$ and $\mathrm{MS+FS}(\lambda_{\mathrm{F1,2}})$ models, it is possible to find an interval of values that satisfy these criteria, which is: $9.2\ \mu\Omega.\mathrm{cm} < \rho_{\mathrm{B,C}}(300\ \mathrm{K}) < 10.0\ \mu\Omega.\mathrm{cm}$ (marked with red stars in Figure S7, Supporting Information). Examples of the obtained modelled curves are shown together with the experimental data at 300 K (Figure 5b) and 20 K (Figure 5c). It can be noticed that p decreases with decreasing temperature, as the e-MFP values are of the same order of magnitude as the film thickness. From these fits, we extract an average reflectivity coefficient $R \approx 0.58 \pm 8.9\%$ and specularity coefficient $p \approx 0.98 \pm 2.0\%$ (at 300 K: $R \approx 0.60 \pm 2.8\%$ and $p \approx 1.00 \pm 0.0\%$).

© 2024 The Author(s). Advanced Engineering Materials published by Wiley-VCH GmbH

15272648, 2025, 4, Downloaded from https://advanced.onlinelibrary.wiley.com/doi/10.1002/adem.202402656, Wiley Online Library on [05/02/2026]. See the Terms and Conditions (https://onlinelibrary.wiley.com/terms-and-conditions) on Wiley Online Library for rules of use; OA articles are governed by the applicable Creative Commons License

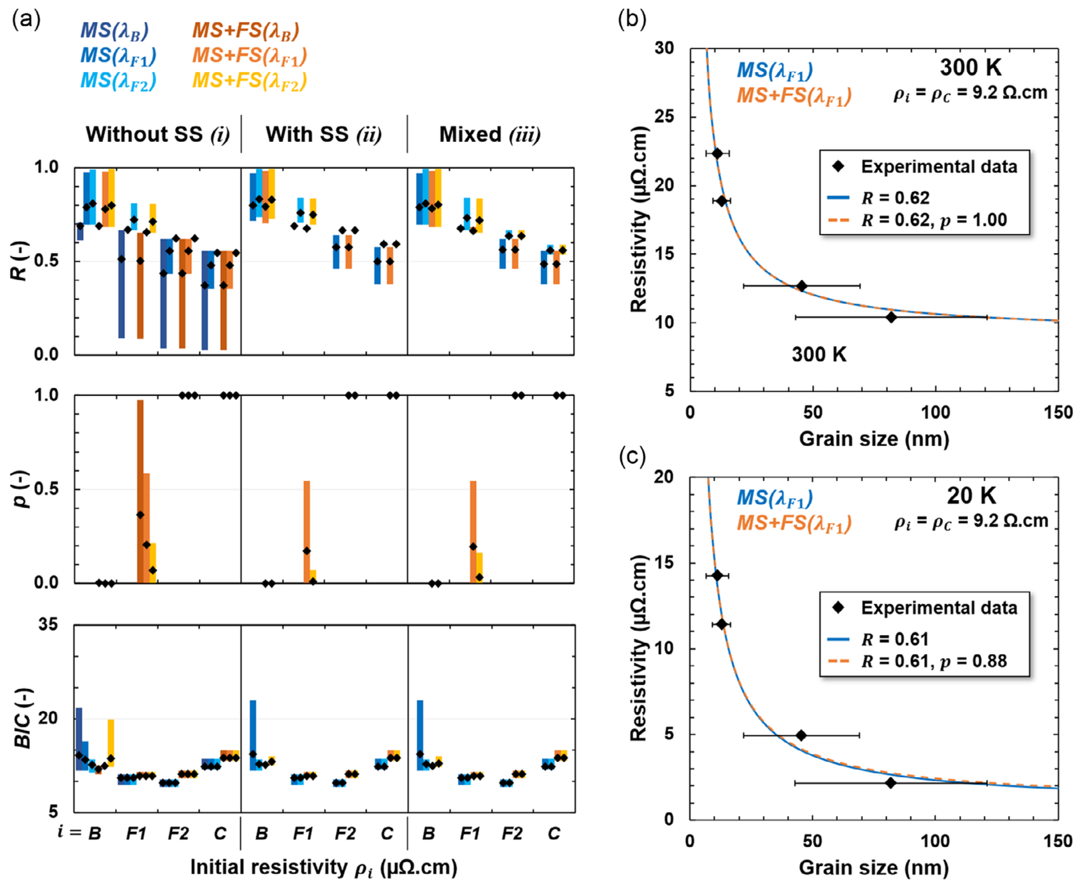

Figure 5. a) Grain reflectivity coefficient R, grain specularity coefficient p and Bayesian information criterion (BIC) as a function of different initial resistivity-temperature curves $\rho i(T)$: bulk (B), film 1 (F1), film 2 (F2) and sample C (C). These values are calculated using MS and MS + FS models, with different e-MFP $\lambda(T)$ considering multiple levels of surface scattering (SS) in the 20–300 K range of temperatures. Diamond points represent the average value over the whole range of temperatures and colored bars show the interval between the minimum and maximum values. Experimental resistivity as a function of the grain size measured at b) 300 K and c) 20 K (diamonds) compared to modeled curves (colored lines) using the appropriate combination of MS(λ_{F1}) and MS + FS(λ_{F1}) models and initial resistivity temperature curves $\rho_i(T)$ (Figure S7, Supporting Information). Their corresponding R and p coefficients are given in the legend.

The obtained R value is in agreement with Zhu et al. who predict the relationship between this specific physical parameter and the melting temperature of different metals (for Ru: $R \approx 0.57$).[38] Except for this study, the reflectivity coefficient for Ru was estimated to be around $R \approx 0.5$, either by indirect determination through the FS model (layers with different thicknesses) or fixed as a free parameter, also in agreement with our results.[3–6,12,13,22–25] Regarding the specularity coefficient p, it is difficult to compare with absolute estimates as it strongly depends on the quality of the layers and interfaces. In our case, it was notably used as a criterion to find a more accurate estimation of R, taking into account our layer quality.

2.3. Failure Modes

Among the studied Ru films, sample C (IT = 40 µs) revealed two different failure modes as illustrated in **Figure 6**a, each one being associated to one specific phenomenon: the buckling and the wrinkling.

Buckling can be observed in both wrinkled and not wrinkled regions. Therefore, this strongly suggests that these two phenomena are not related or neither of them are the consequence or cause of the other one. The most plausible explanation might be that they take part at different length scales: 5–100 nm for the buckling and 200 nm–10 µm for the wrinkling. Moreover, even if they are both consequences of the fast temperature ramps, they can be explained by different phenomenological causes. In the following section, we first describe the wrinkling phenomenon and, then, the buckling phenomenon. It should be noted that cross-sectional and plane view TEM images presented in Section 2.1 have been achieved on the same sample (C), which is fully analyzed in this section. It has been observed on both deformed and nondeformed regions, showing no stack discrepancies and previously described GG enlargement. The aspects highlighted in this section are considered as "failure modes" as they constitute an obstacle for device integration. Thus, the conclusions formulated in the previous sections concerning the structural and electrical

© 2024 The Author(s). Advanced Engineering Materials published by Wiley-VCH GmbH

15272648, 2025, 4, Downloaded from https://advanced.onlinelibrary.wiley.com/doi/10.1002/adem.202402656, Wiley Online Library on [05/02/2026]. See the Terms and Conditions (https://onlinelibrary.wiley.com/terms-and-conditions) on Wiley Online Library for rules of use; OA articles are governed by the applicable Creative Commons License

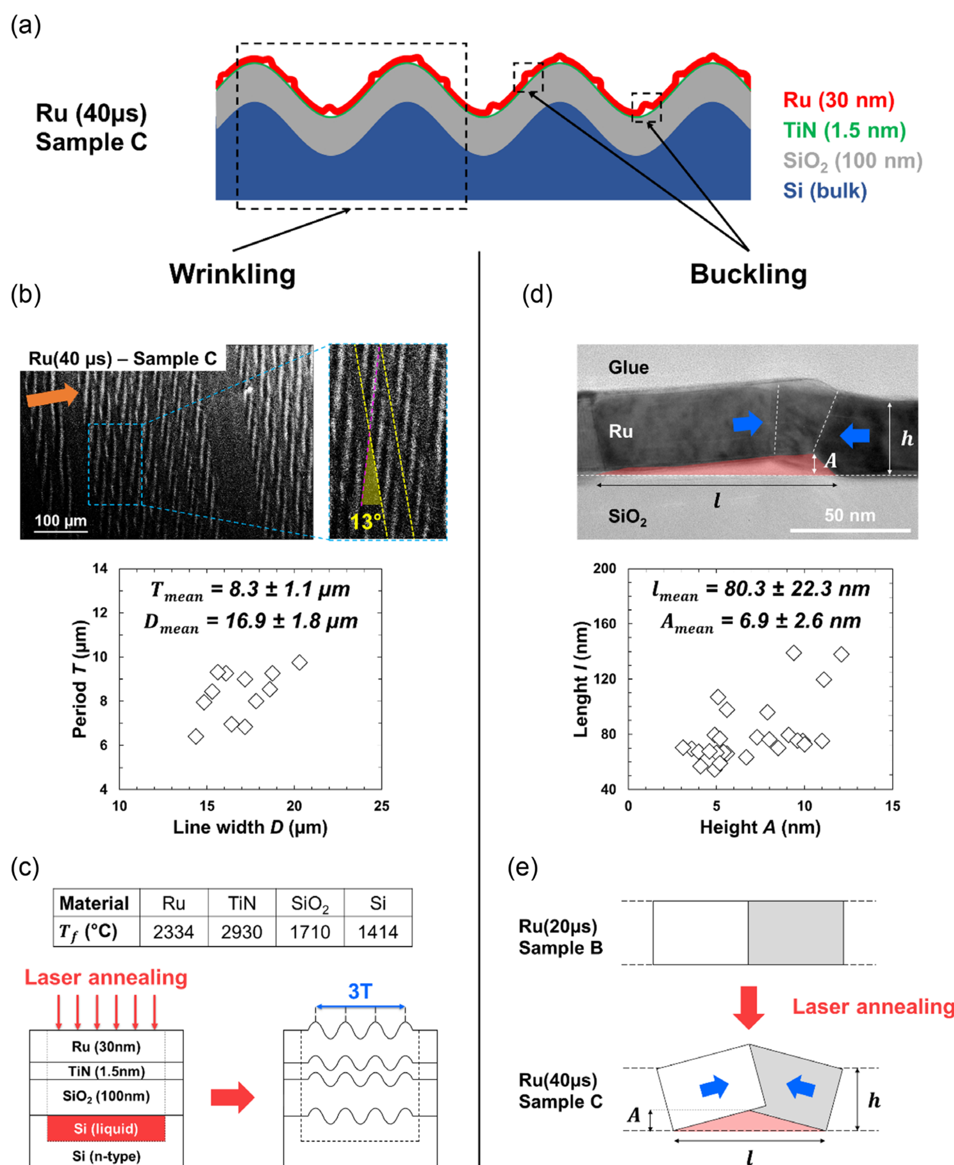

Figure 6. a) Diagram representing the two encountered failure modes in sample C (40 µs): wrinkling and buckling. b) Example of a SEM image illustrating the wrinkling phenomenon along with a zoomed area to show a more accurate view of the wrinkles delimitations (yellow dotted lines). Period T as a function of the line width D measured on multiple wrinkled lines. It has been found that the average period $T_{mean} = 8.3 \pm 1.1$ µm and is not width-dependent. An orange arrow indicates the laser scanning direction. c) Explicative scheme of the wrinkling phenomenon, due to the partial melting of the Si substrate below the Ru/TiN/SiO_2 stack using the laser annealing process. A table summarizing the fusion temperatures T_f of the different materials is also given. d) Example of a TEM image highlighting the buckling phenomenon with the detachment of one grain gliding along a grain boundary. Several delaminated areas have been characterized and their length l versus height A is plotted. These measurements give an average length $l_{mean} = 80.3 \pm 22.3$ nm that is not clearly linked to the height. e) Illustration depicting the buckling phenomenon, originating from film deformation, provoked by compressive strains inside the Ru/TiN film during the laser annealing process. The most probable causes of these strains are the thermal expansion (TE) and the GG.

properties (Figure S8, Supporting Information) remain well founded.

2.3.1. Wrinkles Phenomenon

As shown in Figure 6b, when applying a laser annealing with an IT of 40 µs (sample C), periodic wrinkles arise at the surface. These wrinkles do not cover the surface uniformly but are contained in line-shaped areas (corresponding roughly to the laser beam dimensions), oriented along the same axis but randomly distributed in the perpendicular direction (associated with the scanning direction). Moreover, it can be observed that the wrinkles inside these areas are oriented neither along the line's main axis nor along the scanning direction but with an approximate

© 2024 The Author(s). Advanced Engineering Materials published by Wiley-VCH GmbH

15272648, 2025, 4, Downloaded from https://advanced.onlinelibrary.wiley.com/doi/10.1002/adem.202402656, Wiley Online Library on [05/02/2026]. See the Terms and Conditions (https://onlinelibrary.wiley.com/terms-and-conditions) on Wiley Online Library for rules of use; OA articles are governed by the applicable Creative Commons License

angle of 13° to the lines' axis. A quantitative study has been performed on 12 of these objects using optical microscopy and SEM observations. It was determined that wrinkles have an average line width $D_{mean} = 16.9 \pm 1.8\,\mu m$ and a period $T_{mean} = 8.3 \pm 1.1\,\mu m$, independently of the width variations (Figure 6c). AFM performed in these regions showed wave morphologies with peak-to-peak distances of several hundreds of nanometers, even up to 1.0 μm (Figure S3c, Supporting Information). Similar wrinkles have already been observed for SiO_2/Si stacks annealed by pulsed laser.[39–41] In a precise range of energy densities, a local temperature in between the melt threshold of Si (1414 °C) and SiO_2 (1710 °C) is reached so that, during a few hundred nanoseconds, the silicon dioxide layer stands on a thin liquid silicon layer. Once the heat starts dissipating, silicon recrystallization occurs. Because of mechanical and viscoelastic phenomena, the silicon dioxide layer is bent to finally form periodical wrinkles (or ripples). Moreover, it has been pointed out that the period T of these patterns depends on the SiO_2 layer thickness. Our system is comparable to the outlined one as it includes the SiO_2/Si stack with the addition of the Ru/TiN stack on top of it. Also, we are positioned in a similar configuration regarding the melting temperatures of the materials as the Ru and TiN layers melt at 2334 and 2930 °C, respectively. Considering such stack (equivalent to a silicon dioxide of 130 nm), and by means of the thermal dissipation precise dynamics, the obtained period T is slightly higher but in the same order of magnitude (≈5 μm) as the reported values. In addition to the size of the laser beam, the nonuniform coverage of the surface might arise from a combination of two different causes. First, the corresponding laser condition of sample C (15.0 mJ cm^{-2}, 40 μs) meets closely the temperature profile criterion fulfilling the bulk silicon melt threshold at the SiO_2/Si interface. Second, when positioned in this way at the onset of the silicon melt, the small inhomogeneities of the laser energy profile may be the cause of variations in the distributed ED over the irradiated area. Consequently, the induced variations in temperature at the SiO_2/Si interface could locally satisfy or not the Si melt threshold and so create flat areas with no wrinkles. To understand more precisely the dynamics of the SLA process and confirm this hypothesis, temperature profiles have been calculated using TCAD simulation tools. The results of these simulations are presented and discussed in Section 3. To avoid this phenomenon, the temperature profile must be optimized and two levers can achieve this: the fine-tuning of the laser annealing parameters (ED and IT) and the stack engineering to maximize the temperature in the Ru film while minimizing the one in the Si substrate.

2.3.2. Buckling Phenomenon

Since the mechanical properties involved in such nonequilibrium thermal process have not yet been studied in depth, the following discussion will be based on the observations made with the available characterization methods commonly used. As illustrated in Figure 6a, the buckling phenomenon occurs at the nanometer scale and manifests itself through the Ru layer local delamination from the SiO_2/Si base. Three different TEM cross-sectional lamellas have been prepared to establish a semiquantitative study: two in regions altered by the wrinkles and one in a flat region. The local delamination has been noticed in all three samples, which confirms the buckling phenomenon is not related to the previously described wrinkling. An evaluation of the dimensions involved in this phenomenon has been done by observations over 15 areas. From this analysis, we extracted an average delamination height $A_{mean} = 6.9 \pm 2.6$ nm and length $l_{mean} = 80.3 \pm 22.3$ nm (Figure 6d). Three different scenarios of buckling arise from these observations, all of them entailing one or two grain boundaries (Figure S9a, Supporting Information): 1) the partial detachment of two Ru grains gliding along one grain boundary (Figure 6e), 2) the partial detachment of one grain gliding along one grain boundary, and 3) the detachment of one grain gliding along two grain boundaries. The origin of the buckling might find itself in the mechanical interactions between the Ru/TiN layers and the SiO_2/Si substrate system, whose thermal and mechanical properties differ in many physical quantities. Indeed, their respective average thermal expansion coefficient (TEC) α is (expressed in 10^{-6} K^{-1}, in **Table 1**): 9.6 (Ru), 10.0 (TiN), 1.0 (SiO_2), and 3.0 (Si). Considering the SiO_2 layer as the base thick layer (100 nm) for the Ru/TiN stack (31.5 nm) and that the whole stack goes through an equivalent temperature rise (up to 1500 °C), their TEC differs by around one order of magnitude. This means that while the Ru/TiN layers require space to expand, the SiO_2 layer is imposing its own TE. Consequently, this situation is likely to generate a significant horizontal compressive stress inside the Ru/TiN films. A STEM–EDX analysis in a delaminated region qualitatively confirmed the simultaneous buckling of the TiN and Ru layers (Figure S9b, Supporting Information).

In our case, the release of this stress occurs along the grain boundaries with a gliding phenomenon that tends to shift a part of the volume of the film in the out-of-plane direction. This would suggest that the metallic bonds present at the grain boundaries are weaker than the covalent bonds in the grains. Also, regarding sample C, besides the fast nature of the pulsed laser annealing dynamics, the buckling phenomenon might even be enhanced by the concomitant grain enlargement, and thus the reduction of the grain boundary density. Indeed, for a given compressive stress, it would be easier to keep the integrity of the layer by having a high density of grain boundaries than with a low

Table 1. Thermal and mechanical characteristics of Ru, TiN, SiO_2, and Si: TEC α, Young's modulus E, and Poisson ratio ν.

Material[a)]	TEC α [10^{-6} K^{-1}]	Young's modulus E [GPa]	Poisson ratio ν [–]
Ru[23,53–61]	5.1–20.1	400–560	0.21–0.30
	(9.6)	(450)	(0.25)
TiN[62–67]	9.4–28.0	245–590	0.23–0.25
	(10.0)	(400)	(0.24)
SiO2[68–75]	0.4–4.0	60–75	0.15–0.25
	(1.0)	(70)	(0.20)
Si[76–84]	2.5–5.0	100–200	0.15–0.80
	(3.0)	(150)	(0.30)

[a)] Most representative average values are given in parentheses.

© 2024 The Author(s). Advanced Engineering Materials published by Wiley-VCH GmbH

15272648, 2025, 4, Downloaded from https://advanced.onlinelibrary.wiley.com/doi/10.1002/adem.202402656, Wiley Online Library on [05/02/2026]. See the Terms and Conditions (https://onlinelibrary.wiley.com/terms-and-conditions) on Wiley Online Library for rules of use; OA articles are governed by the applicable Creative Commons License

density, as the force per unit area would be less distributed. The buckling strain threshold can be evaluated through different calculations. Based on the work of Hutchinson and Suo,[42–45] we can evaluate an upper value of this threshold through the given formula (Equation (5)):

$$\sigma_{\mathrm{B}} = E \times \varepsilon_{\mathrm{B}} = E \times \frac{\pi^2}{12}\left(\frac{2h}{l}\right)^2 \tag{5}$$

with the Young's modulus E, the film thickness h, and the buckling length l. Considering our values of the buckling length, we obtain $\sigma_{\mathrm{B}} \approx 200$ GPa. As this theory neglects several phenomena, notably the elastic deformation in the substrate, it is known to largely overestimate the critical strain value for buckling. Here, we propose to roughly determine the buckling strain threshold by using data from samples B and C, as this phenomenon emerges between these two lasers annealing conditions. Two simultaneous contributions to the buckling are taken into account: the TE and the GG, both of them being spatially restricted by the SiO_2/Si substrate layers. The horizontal strain coming from TE and GG can be written as (Equation (6) and (7))[46]

$$\sigma_{\mathrm{TE}} = E \times \varepsilon_{\mathrm{TE}} = E \times \alpha \Delta T \tag{6}$$

$$\sigma_{\mathrm{GG}} = E \times \varepsilon_{\mathrm{GG}} = E \times \frac{\delta\beta}{2(1-\nu)}\left(\frac{1}{g_0} - \frac{1}{g}\right) \tag{7}$$

with the temperature change ΔT, the grain boundary thickness δ, the relative density difference between the bulk and grain boundary β, the Poisson ratio ν, the initial grain size g_0, and the resulting grain size after subsequent laser annealing g. The total horizontal strain σ_{T} is given by (Equation (8))[47,48]

$$\sigma_{\mathrm{T}} = \sigma_{\mathrm{TE}} + \sigma_{\mathrm{GG}} \tag{8}$$

For both sample B and C, the grain boundary thickness and the relative density difference between the bulk and grain boundary have been set to $\delta \approx 0.4$ nm (evaluated thanks to TEM cross-sectional images) and $\beta \approx 0.5$ (due to the observed gliding). All the grain size values are taken from the average grain size values discussed in Section 2.1: $g_0 = 11.1$ nm (reference), $g_{\mathrm{B}} = 45.4$ nm (sample B), and $g_{\mathrm{C}} = 81.9$ nm (sample C). The temperature changes are estimated around $\Delta T_{\mathrm{B}} \approx 1400$ K and $\Delta T_{\mathrm{C}} \approx 1500$ K (see next section, **Figure 7**a). We finally have $\sigma_{\mathrm{TB}} \approx 10.1$ GPa and $\sigma_{\mathrm{TC}} \approx 11.1$ GPa. These values give a first range of the buckling strain threshold σ_{B} of our system, which is around 20 times lower than predicted by the Hutchinson and Suo theory. The relation between the buckling amplitude (or delamination height) A and the buckling strain threshold σ_{B} (Equation (9)) has been obtained analytically in previous studies:[42]

$$A = \frac{2h}{\sqrt{3}}\sqrt{\frac{\sigma_{\mathrm{T}}}{\sigma_{\mathrm{B}}} - 1} \tag{9}$$

From the measured buckling amplitude A_{mean} and the estimated total horizontal strain σ_{TC} in sample C, we can deduce $\sigma_{\mathrm{B}} \approx 10.7$ GPa. Using this formula, we can evaluate that the strain conditions exceed the buckling threshold of about 4–5%. Between samples B and C, the strain contribution originating from the TE increases from ≈49% to ≈58% while the one from GG decreases from ≈51% to ≈42%. This suggests that, despite the absolute strain increase due to GG, TE is expected to be the dominant phenomenon at high temperatures and, therefore, the main cause of the buckling.

3. Process Simulations and Perspectives

3.1. Simulation Tool

Numerical simulation of the microsecond laser annealing process is challenging since it involves phase change and related sub-µs scale diffusion phenomena. In this context, a finite element method based on computational tools dedicated to the simulation of laser annealing process for 1D, 2D, and 3D structures has been developed. It is a complete TCAD package, called LASSE Innovation and Application Booster (LIAB), described thoroughly in the literature.[10,40,49,50] LIAB self-consistently solves multiple equations: the heat equation coupled to the time-harmonic solution of Maxwell equations (laser light coupling), the phase field equation, and the diffusion equation. The equation solving also includes several material properties such as the transition temperatures of its different phases, depending on the composition when the considered material is an alloy. In our study, no alloys are used and no species diffusion is observed. Our system can then be simulated using the following heat and phase field Equation (10) and (11):

$$\rho c_{\mathrm{p}} \frac{\partial T}{\partial t} = \nabla[k(T,\varphi)\nabla T \nabla] + 30\varphi^2(1-|\varphi|^2)L\frac{\partial \varphi}{\partial t} + S(r,t) \tag{10}$$

$$\begin{aligned}\frac{\partial \varphi}{\partial t} = {} & W\nabla^2(\varphi) - 2\varphi(1-|\varphi|)(1-2|\varphi|) \\ & - 8\lambda(T,\varphi)\left[T - T_f\right]\varphi^2(1-|\varphi|)^2\end{aligned} \tag{11}$$

with the time step t, the position r, the material phase $\varphi \in [-1,1]$ (with -1 being the pure liquid phase and 1 the pure solid phase), the fusion temperature T_{f}, the latent heat of fusion L, and the heat capacity c_{p}, conductivity k, and density ρ, respectively. The parameters W and λ are the phase field parameters chosen in order to achieve the thin interface limit. The $S(r,t)$ function is the heat source due to the absorption of laser light and is determined by solving both Equation (12) and (13), the latter being the Maxwell equation in the time-harmonic approximation:[50]

$$S(r,t) = P(t)k_0\varepsilon_i|E(r,t)|^2 \tag{12}$$

$$\nabla(\nabla E(r,t)) - k_0\varepsilon_i|E(r,t)|^2 = 0 \tag{13}$$

with the electric field E, the time-dependent incident laser power $P(t)$, the incident plane wavevector in vacuum k_0, and the imaginary part of the dielectric constant of the material ε_i.

© 2024 The Author(s). Advanced Engineering Materials published by Wiley-VCH GmbH

15272648, 2025, 4, Downloaded from https://advanced.onlinelibrary.wiley.com/doi/10.1002/adem.202402656, Wiley Online Library on [05/02/2026]. See the Terms and Conditions (https://onlinelibrary.wiley.com/terms-and-conditions) on Wiley Online Library for rules of use; OA articles are governed by the applicable Creative Commons License

15272648, 2025, 4, Downloaded from https://advanced.onlinelibrary.wiley.com/doi/10.1002/adem.202402656, Wiley Online Library on [05/02/2026]. See the Terms and Conditions (https://onlinelibrary.wiley.com/terms-and-conditions) on Wiley Online Library for rules of use; OA articles are governed by the applicable Creative Commons License

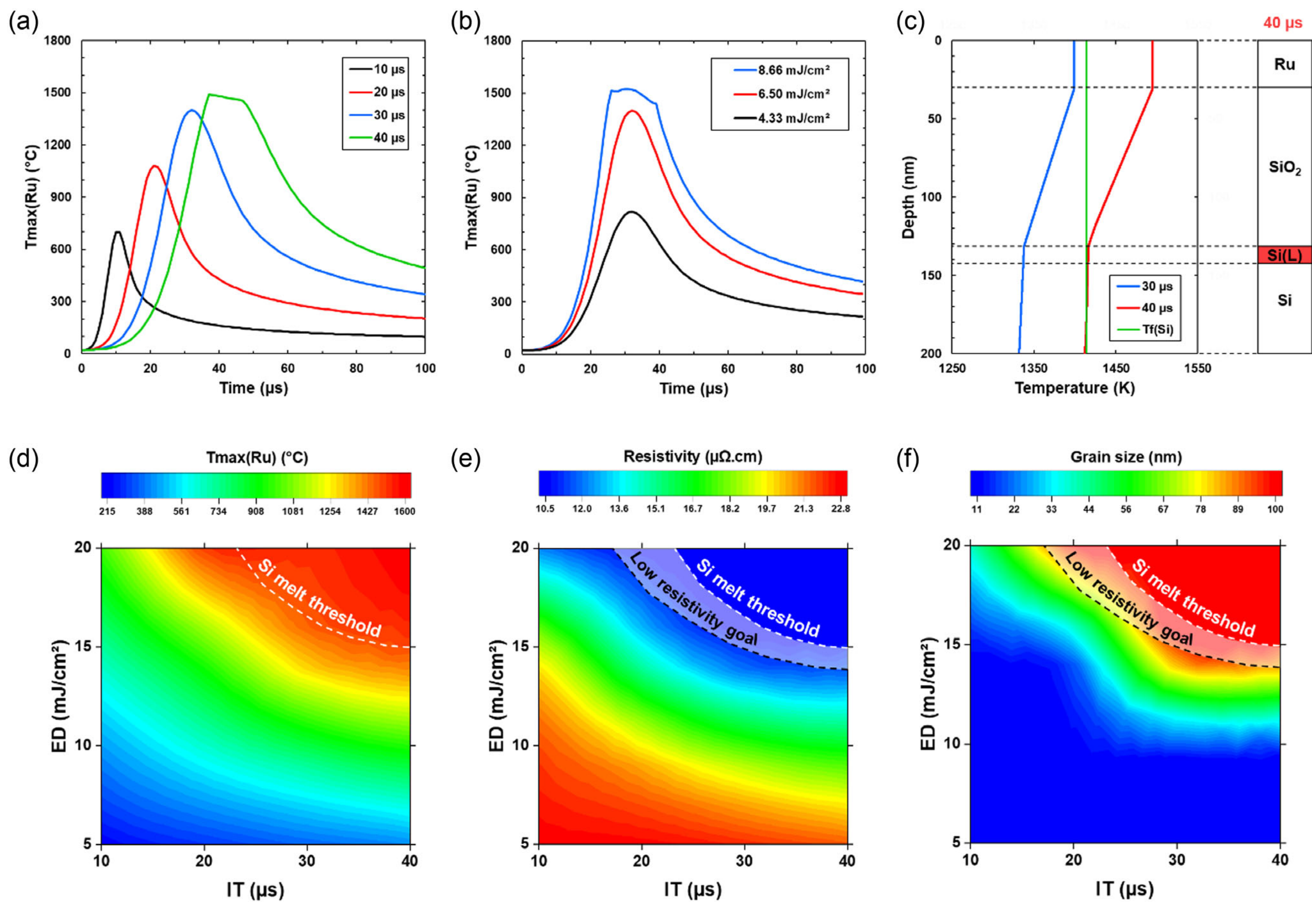

Figure 7. Simulated temporal evolution of maximum temperature profiles T_{max} inside a 30 nm thick Ru film (using LIAB tool): a) for a fixed ED (6.50 mJ cm^{-2}) and different IT (ΔIT = 10–40 µs) and b) for a fixed IT (30 µs) and different ED (ΔED = 4.33–8.66 mJ cm^{-2}). c) Simulated maximum temperature depth profiles extracted at the Si peak temperature for two different ITs (30 and 40 µs) for a fixed ED of 4.33 mJ cm^{-2}. For an IT = 40 µs, a 30 nm thick Si liquid layer (Si(L)) below the SiO_2/Si interface is formed, confirming the origin of the wrinkles. d) ED versus IT mapping of the simulated maximum temperature inside the Ru film. A white dotted line delimits the conditions involving the melting of the silicon substrate. e) ED versus IT mapping of the measured Ru resistivities. In addition to the Si melt threshold demarcation, a black dotted line is added to highlight the lowest reachable resistivity values. f) ED versus IT mapping of the grain size, calculated from e) using the best modelled curves at 300 K (Figure 5b).

3.2. Results and Discussions

3.2.1. Influence of the SLA Parameters on the Maximum Temperature Profiles in Ru Films

As mentioned in previous sections, the SLA process can be tuned through the IT and the ED parameters, thereby influencing temperature profile, temporally and spatially. Thanks to the LIAB simulation tool, the experimental system was reproduced and the impact of the two previously mentioned parameters on the temporal evolution of the maximum temperature T_{max} in the Ru film was examined. To that purpose, ED and IT conditions close to the experimental conditions were selected. In Figure 7a, we show different $T_{max}(t)$ curves corresponding to different IT for a fixed ED (ED = 6.5 mJ cm^{-2}, ΔIT = 10–40 µs) and conversely in Figure 7b (IT = 30 µs and ΔED = 4.33–8.66 mJ cm^{-2}). As expected, the temperature values of the T_{max} profiles rise when increasing ED (and IT, respectively). However, depending on the fixed parameter, two slightly different behavior can be observed. For a fixed IT (Figure 7b), the increase in temperature occurs with the same maximum temporal position while, for a fixed ED (Figure 7a), the maximum is shifted toward higher time values. Also, the variation in IT has a clear impact on the temperature ramp: the lower the IT, the faster the temperature peak is attained. This is due to the transmitted power ramp dP/dt (dt being directly proportional to the IT) that is higher for short than for long IT. Moreover, the curves associated with 40 µs in Figure 7a and with 8.66 mJ cm^{-2} in Figure 7b display a plateau at their maximum temperature values. This phenomenon is related to the melting occurring in the Si substrate (latent heat), stabilizing the temperature of the whole stack.

3.2.2. Wrinkles Phenomenon

As mentioned in the previous section dedicated to failure modes, when reaching IT = 40 µs at ED = 15.0 mJ cm^{-2}, line-shaped area with wrinkles appears at the surface (Figure 7a,c).

 © 2024 The Author(s). Advanced Engineering Materials published by Wiley-VCH GmbH

The formulated hypothesis for the formation of such surface asperities was that the Si substrate underneath the SiO_2 layer might have become liquid during a short time, leading to the formation of wrinkles after the recrystallization process, as already reported in the literature.[39,40,51,52] Using LIAB simulations, it is possible to probe the evolution of the temperature at the SiO_2/Si interface over time and for different laser conditions. Figure 7c shows the simulated temperature profile as function of depth inside the system when the maximum temperature is reached at the SiO_2/Si interface for two different IT conditions (30 and 40 μs) at $ED = 4.33\ mJ\ cm^{-2}$. Contrary to the 30 μs condition, at 40 μs, the temperature inside a 30 nm thick Si layer below the silicon dioxide exceeds the Si melting point (1414 °C) and becomes momentarily liquid. This confirms our hypothesis and the relevance of LIAB simulation tool. To calibrate the simulated to experimental ED, we applied a correction coefficient $\gamma \approx 2.3$ to the simulated ED ($ED(simu) = 6.5\ mJ\ cm^{-2}$ corresponding to $ED(exp) = 15.0\ mJ\ cm^{-2}$).

3.3. Further Process Optimizations

The laser conditions studied in Figure 7c confirmed the relevant calibration of the simulation model thanks to the good agreement between the simulation and the experimental results. Based on the same model, multiple combinations of ED and IT laser conditions were used to evaluate the other possible process windows. In Figure 7d, the peak temperature inside the Ru film is plotted as function of the ED and IT. The laser conditions involving the melting of the Si substrate, and so the apparition of the wrinkling phenomenon, are delimited by the black dotted line. The conditions outside this area are suitable for device fabrication and should allow to avoid failure modes, or at least the surface wrinkles. The simulated conditions have been performed experimentally and their corresponding resistivity have been measured. From simulations and experiments, we can identify a process window giving simultaneously the minimum of resistivity and no wrinkles (correlated to the Si melting threshold). This process window is illustrated by the hatched area in Figure 7e, which represents the resistivity evolution as function of ED and IT. In the section dedicated to the electrical properties of our Ru films, the relationship between the average grain size and the resistivity at 300 K was analytically determined by using the MS and MS + FS models (Figure 5b). This interdependence has been used to extrapolate the resistivity values presented in Figure 7e into their corresponding average grain size values, presented in Figure 7f. Thus, to achieve the ideal process window, the average grain size should be comprised between 80 and 100 nm. A future design of experiment will be implemented to prove the good agreement between the experimental and the simulated grain size.

4. Global Perspectives on Ru and Laser Annealing for Future Technology Nodes

The combination of the fast and local laser annealing process with the remarkable Ru material allowed tackling several relevant questions about both topics. In this section, we gather further developments and questions related to the laser annealing technique and the integration of Ru in the future devices that arises from our work. Part of these issues might be addressed separately, either from a process point of view independently of the studied material or from the Ru perspective regardless of the annealing technique.

4.1. Scanning Microsecond UV Laser Annealing (SLA)

4.1.1. ED Parameter

The choice of the ED is crucial for such laser process entailing a cumulative thermal budget through the multipulse distinctive feature. In comparison with noncumulative laser tools, high ED in SLA can significantly reduce the thermal process duration, which is suitable for large-scale integration. In addition to the strict requirements in reproducibility and process window precision over large areas, it is essential to reflect on the equivalence between the two extreme laser conditions, i.e., "high ED, low IT" and "low ED, high IT". In this work, choosing the "high ED, low IT" strategy leads to a considerable grain size enlargement although with a large lognormal distribution. This result might be the cause of electrical discrepancies noticeable through a minimum reachable resistivity value higher than expected. The opposite "low ED, high IT" strategy should be compared to the studied "high ED, low IT" conditions to examine its impact on the grain size evolution.

4.1.2. Extension of the Process Window

Aside from the ED parameter, other intrinsic and external parameters could be considered as good process levers. Two different parameters might be for instance: the multiplication of the number of scans and the background temperature (e.g., with a heating chuck), as a supplement to the cumulative feature of the SLA. Furthermore, but harder to achieve, operating at a different working frequency could open new opportunities.

4.1.3. Incorporation of Mechanical Properties in Simulation Tools

In most studies involving heating techniques, the electrical and structural properties of a material are correlated. The fast and intense aspects of the temperature profiles produced by the laser annealing process are likely to generate mechanical deformation, particularly when multiple layers of different materials are irradiated. For further laser process optimization or even exploration, the incorporation of the mechanical characteristics and their merging with the structural and electrical properties of materials are required and may be strongly beneficial. Indeed, filling this part of the laser annealing process dynamics might open new process windows to consider and open new solutions for future devices.

4.2. Ruthenium and Future Metals for Interconnections

4.2.1. Electrical Analysis

Thanks to our laser annealing process, four different samples with unique resistivity versus temperature characteristics were fabricated, highlighting different electron–phonon dependencies. To take this assessment into account, a variation of the

© 2024 The Author(s). Advanced Engineering Materials published by Wiley-VCH GmbH

15272648, 2025, 4, Downloaded from https://advanced.onlinelibrary.wiley.com/doi/10.1002/adem.202402656, Wiley Online Library on [05/02/2026]. See the Terms and Conditions (https://onlinelibrary.wiley.com/terms-and-conditions) on Wiley Online Library for rules of use; OA articles are governed by the applicable Creative Commons License

MS model was used, including e-MFP versus temperature properties along with possible surface scattering phenomenon and variations of the initial resistivity. To validate the robustness of this new approach, more calculations need to be done on a larger number of samples (resistivity vs grain size data points) and on different materials.

4.2.2. Scalability

Despite their highlighted reliable electrical quality, it should be pointed out that the best obtained Ru resistivity (10.4 μΩ cm) remains higher than the expected Cu resistivity (≈3.0 μΩ cm) for 30 nm thick films.[28] However, one must keep in mind the scalability of Ru over Cu, not only for thinner films but more importantly on patterned interconnections.[27] In such structures, SLA should be considered as a major low-temperature process, thanks to its fast and local thermal budget.[25] With this in mind, exploring the interaction between SLA and designed interconnections is essential.

4.2.3. Failures Modes

As discussed in the section dedicated to simulations, wrinkling can be easily avoided by using conditions that do not provoke the melting of the Si substrate. This can be achieved by identifying the related threshold (by experiment or simulation) and working outside this process window. However, the wrinkling and the buckling being independent from each other, the latter can appear in the appropriate process window defined for the former. Inconveniently, the buckling cannot be clearly predicted by physical models or simulations, but only seen through experimental attempt. However, apart from the incorporation of the mechanical properties into the simulation tools, practical solutions can be found and further experiments can be performed. In a long-term strategy, further experiments could be conducted to acquire a more accurate understanding of the phenomenon, for instance, its precise activation or variations depending on the applied thermal budget. Such design of experiment would certainly provide a better understanding not only on the buckling but also on the mechanical properties of Ru upon pulsed laser annealing (applicable to all other materials). In the short-term, this phenomenon could be countered by using a capping layer to constrain the Ru both from the bottom and top interfaces or a different dielectric material that is both adapted to the mechanical properties of Ru/TiN films and can fulfil the insulating properties requirements. In addition to the use of suitable materials, the laser annealing conditions can be tuned to reduce the probabilities of triggering the buckling, especially by decreasing the temperature gradient during the process, for instance with a "low ED, long IT" strategy.

5. Conclusion

In this work, we studied the electrical and structural properties of 30 nm thick Ru thin films deposited on a $TiN/SiO_2/Si$ stack and annealed by UV microsecond laser annealing. In addition to its appropriate technology compatible features, that is to provide a fast and local thermal budget, we showed that SLA is a relevant technique for the improvement of Ru thin films properties, which are critical for future BEOL interconnections scalability. Selecting one ED and different ITs, we demonstrated by TEM observations that by increasing the thermal budget a significant grain enlargement was achieved. Three regimes are noticeable, from almost no GG, to linear increase with the thermal budget increase, to saturation. The initial average grain size of the physical vapor deposition (PVD) Ru layer increased from 11.2 ± 4.6 to up to 81.9 ± 39.1 nm, turning the distribution from Gaussian to lognormal. When applying low thermal budgets, the Ru layer is constituted by randomly superimposed small grains, whereas, for high enough thermal budget conditions, we observe large grains occupying the whole 30 film thickness with grain boundaries perpendicular to the layer interfaces. The larger the grains, the lower the grain boundary density and, consequently, the higher the conductivity (up to a 53% improvement). Measured by 4PP and Van der Pauw methods, the resistivity trends show three regimes when increasing the thermal budget, similar to the evolution of the grain size. It has been emphasized that the resistivity improvement does not follow rigorously the grain size enlargement but with a certain interval in the IT: the resistivity drops abruptly while the grain size growth has not properly started and reaches its asymptotic minimal value although the GG has not yet saturated. This behavior is characteristic of the MS model describing the resistivity as a function of the grain size. With the support of resistivity versus temperature measurement, it has been demonstrated that each irradiated sample presented different electron–phonon dependencies, thus impacting their respective electron mean free path. A variation of the standard MS model considering temperature-dependent e-MFP along with varying initial resistivity curves allowed consistent results to be obtained. To confirm the robustness of this model, we encourage the use of this model in future equivalent studies, possibly with a higher number of data points. For resistivity measurements performed between 20 and 300 K, and using the straightforward MS model and its alternative combining it with the FS model (SS), we evaluate an average reflectivity coefficient $R \approx 0.58 \pm 8.9\%$ and a specularity coefficient $p \approx 0.98 \pm 2.0\%$, in agreement with the literature. This result is also consistent with the quality of our films, demonstrating the negligible influence of the surface scattering phenomenon (low surface roughness and low Ru e-MFP compared to film thickness, particularly at 300 K). For significant thermal budget (long ITs), our system exhibits two failure modes for device fabrication: the wrinkling and the buckling, occurring at two different scales, micrometer and nanometer, respectively. The wrinkling originates from the partial melting of the Si substrate below the Si/SiO_2 interface and the period of the surface wrinkles is in the same order of magnitude as already observed in previous studies for a SiO_2/Si system. The buckling can be explained by the considerable difference in TEC between the Ru/TiN and SiO_2/Si layers. Indeed, due to the large temperature gradients involved during the laser annealing process, Ru and TiN layers are compressively strained above a mechanical threshold, forcing both layers to locally delaminate. The simulation of such thermal processes, results, and phenomena is required to reach future technology nodes at lower cost. Using standard TCAD packages, a simulation tool interfacing the laser annealing process with materials has been developed. Thanks to this

© 2024 The Author(s). Advanced Engineering Materials published by Wiley-VCH GmbH

15272648, 2025, 4, Downloaded from https://advanced.onlinelibrary.wiley.com/doi/10.1002/adem.202402656, Wiley Online Library on [05/02/2026]. See the Terms and Conditions (https://onlinelibrary.wiley.com/terms-and-conditions) on Wiley Online Library for rules of use; OA articles are governed by the applicable Creative Commons License

simulation module, temperature profiles inside the system studied could be simulated, confirming the Si melting as the root cause of the wrinkling phenomenon. Moreover, combining measurements and simulations, further process windows have been identified to avoid the triggering of the wrinkling while giving the best resistivity values. The results suggest that such process window corresponds to an average grain size between 80 and 100 nm. As the mechanical properties are not yet incorporated in the simulation tools, we cannot predict the apparition of the buckling depending on the selected laser annealing conditions. We consider this as a major lack for the field of thermal processes as well as for the development of future technologies and, consequently, one that must be rapidly addressed. Once placed in the suitable process window, we proved that SLA allows to improve by 53% the Ru film resistivity down to the noteworthy value of 10.4 $\mu\Omega$ cm. Despite being still higher than the equivalent best 30 nm thick Cu layer ($\approx$3.0 $\mu\Omega$ cm), scalability must be kept in mind especially when considering patterned structures, as already demonstrated. Accordingly, this study constitutes a decisive step forward in the reliable integration of Ru in future BEOL interconnections.

6. Experimental Section

Fabrication Process and Laser Annealing System: 30 nm thick Ru layers were deposited by PVD at RT, on top of a 1.5 nm thick TiN layer grown by atomic layer deposition at 450 K and a 100 nm thick SiO_2 oxide layer fabricated by thermal oxidation. This three-layers stack was fabricated on a 300 mm Si(100) wafer substrate and each thickness was chosen to mimic the BEOL system as accurately as possible. The TiN layer was used as a diffusion barrier to avoid Ru, Si, and O intermixing and so to prevent the Ru film from being contaminated during the SLA process. Moreover, the SiO_2 layer emulated the standard dielectric layer that insulated adjacent metal interconnections. The whole stack was then annealed by SLA thanks to a SCREEN-LASSE system, using monochromatic laser with an operating wavelength between 300 and 400 nm and operating at RT under a nitrogen (N2) flow. Given the high-frequency feature of the used laser tool, applying different thermal budgets can be achieved by varying the IT and the ED. For each selected conditions, several back-and-forth laser scans were performed to finally irradiate 15×15 mm^2 areas. In this study, we explored various values of IT between 1 and 40 µs while maintaining a constant ED of 15.0 mJ cm^{-2}.

Characterization and Analysis Methods: Several characterization methods were used to investigate the Ru layers. The investigations on the conductivity were conducted using the 4PP measurement method with a 333A semiautomatic 4-point in-line measurement system from Microworld and a SUSS Microtec PA200 probe station combined with an Agilent 4142B source/monitor system. Temperature measurements of the resistivity down to 20 K have been performed by combining a Hall effect HL5500PC system from Nanometrics, a homemade cryochamber and a He compressor. The structural properties of the layers were studied by scanning TEM (STEM) and conventional TEM working with two different microscopes. For the STEM, both bright field (BF) and HAADF modes were used (not shown). The conformity and crystallinity of the stack were confirmed with cross-sectional observations by standard and HR-TEM imaging, using a JEOL JEM-ARM200F equipped with a cold FEG source and a probe corrector. Chemical analysis to check the absence of species intermixing was performed by EDX thanks to a CENTURIO-X SDD detector on the same microscope. The evolution of the grain size and crystallinity was studied by plan view imaging with a JEOL JEM 2100F. Cross-sectional samples were prepared with focused ion beam Helios 600i from field electron and ion company while plan view samples were fabricated via mechanical polishing followed by ion milling. Prior to the cross-sectional cutting procedure, a protective carbon layer was electrodeposited. Investigations about the grains orientations and crystalline phases were conducted by XRD in GI configuration, thanks to a Bruker D8 Discover diffractometer (Cu Kα_1, $\lambda = 1.54$ Å). Also, the surface morphology of the layers was examined by AFM in tapping mode with a Veeco Dimension (2×2 μm^2 scans). MATLAB was used to extract physical parameters by fitting the electrical measurements with existing physical models.

Supporting Information

Supporting Information is available from the Wiley Online Library or from the author.

Acknowledgements

The authors gratefully acknowledge funding from the European Union's Horizon 2020 Research and Innovation program under grant agreement no. 875999-2 IT2. This work was supported by the LAAS-CNRS micro- and nanotechnologies platform, a member of the RENATECH French national network. The authors would like to thank the Institute of IMEC, SCREEN-LASSE company (Gennevilliers) and CASTAING microscopy platform (Toulouse) for their network and facilities involving film deposition, laser annealing process, electrical measurements, and TEM observations. The authors also want to recognize Lucie Albert for the help in the electrical modeling using MATLAB programming and numeric computing platform. The authors dedicate this article in loving memory of their friend and colleague Fuccio Cristiano, who passed away in January 2024, for his contribution to the foundation of this project.

Conflict of Interest

The authors declare no conflict of interest.

Author Contributions

Richard Daubriac: data curation (lead); formal analysis (lead); investigation (lead); methodology (lead); project administration (lead); software (lead); supervision (lead); validation (lead); writing—original draft (lead); writing—review & editing (lead). **Leonardo Cancellara**: data curation (equal); formal analysis (equal); investigation (equal); methodology (equal); writing—review & editing (equal). **Zeinab Chehadi**: data curation (equal); formal analysis (equal); investigation (equal); methodology (equal); writing—review & editing (supporting). **Lu Lu**: data curation (equal); formal analysis (equal); investigation (equal); methodology (equal); writing—review & editing (supporting). **Louis Thuries**: data curation (equal); formal analysis (equal); investigation (equal); methodology (equal); writing—review & editing (supporting). **Mohamed Ali Khaled**: data curation (supporting); formal analysis (supporting); investigation (supporting); methodology (supporting); writing—review & editing (equal). **Fabien Roze**: data curation (supporting); formal analysis (supporting); writing—review & editing (equal). **Nicolas Jourdan**: conceptualization (equal); data curation (supporting); formal analysis (supporting); writing—review & editing (supporting). **Zsolt Tokei**: conceptualization (equal); data curation (supporting); formal analysis (supporting); writing—review & editing (supporting). **Armel Descamps-Mandine**: data curation (supporting); formal analysis (supporting); investigation (supporting); methodology (supporting); writing—review & editing (supporting). **Teresa Hungria**: data curation (supporting); formal analysis (supporting); investigation (supporting); methodology (supporting); writing—review & editing (supporting). **Pier-Francesco Fazzini**: data curation (supporting); formal analysis (supporting); investigation (supporting); methodology (supporting). **Toshiyuki Tabata**: data curation (equal); formal analysis (equal); funding acquisition (lead); investigation (equal); methodology (equal); supervision (supporting); validation (equal); writing—review & editing (equal). **Karim**

© 2024 The Author(s). Advanced Engineering Materials published by Wiley-VCH GmbH

15272648, 2025, 4, Downloaded from https://advanced.onlinelibrary.wiley.com/doi/10.1002/adem.202402656, Wiley Online Library on [05/02/2026]. See the Terms and Conditions (https://onlinelibrary.wiley.com/terms-and-conditions) on Wiley Online Library for rules of use; OA articles are governed by the applicable Creative Commons License

Huet: data curation (equal); formal analysis (equal); investigation (equal); methodology (equal); supervision (supporting); validation (equal); writing—original draft (equal); writing—review & editing (supporting).

Data Availability Statement

The data that support the findings of this study are available from the corresponding author upon reasonable request.

Keywords

buckling, grain size enlargement, pulsed laser annealing, resistivity, wrinkling

Received: November 12, 2024
Published online: January 7, 2025

[1] S. Dutta, K. Moors, M. Vandemaele, C. Adelmann, *IEEE Electron Device Lett.* **2018**, *39*, 268.
[2] C.-K. Hu, J. Kelly, H. Huang, K. Motoyama, H. Shobha, Y. Ostrovski, J. H.-C. Chen, R. Patlolla, B. Peethala, P. Adusumilli, T. Spooner, R. Quon, L. M. Gignac, C. Breslin, G. Lian, M. Ali, J. Benedict, X. S. Lin, S. Smith, V. Kamineni, X. Zhang, F. Mont, S. Siddiqui, F. Baumann, in *2018 IEEE Int. Reliability Physics Symp. (IRPS)*, Burlingame, CA **2018**, pp. 4F.1-1–4F.1-6.
[3] X. Zhang, H. Huang, R. Patlolla, F. W. Mont, X. Lin, M. Raymond, C. Labelle, E. T. Ryan, D. Canaperi, T. E. Standaert, T. Spooner, G. Bonilla, D. Edelstein, in *2017 IEEE Int. Interconnect Technology Conf. (IITC)* **2017**, pp. 1–3.
[4] S. Dutta, S. Kundu, L. Wen, G. Jamieson, K. Croes, A. Gupta, J. Bömmels, C. J. Wilson, C. Adelmann, Z. Tőkei, in *2017 IEEE Int. Interconnect Technology Conf. (IITC)* **2017**, pp. 1–3.
[5] L. G. Wen, C. Adelmann, O. V. Pedreira, S. Dutta, M. Popovici, B. Briggs, N. Heylen, K. Vanstreels, C. J. Wilson, S. Van Elshocht, K. Croes, J. Bömmels, Z. Tőkei, in *2016 IEEE Int. Interconnect Technology Conf./Advanced Metallization Conf. (IITC/AMC)* **2016**, pp. 34–36.
[6] D. Wan, S. Paolillo, N. Rassoul, B. K. Kotowska, V. Blanco, C. Adelmann, F. Lazzarino, M. Ercken, G. Murdoch, J. Bömmels, C. J. Wilson, Z. Tökei, in *2018 IEEE Int. Interconnect Technology Conf. (IITC)*, San Jose, CA **2018**, pp. 10–12.
[7] G. Fortunato, L. Mariucci, A. Pecora, V. Privitera, F. Simon, in *Laser Annealing Processes in Semiconductor Technology* (Eds: F. Cristiano, A. La Magna), Woodhead Publishing, Cambridge, Cambridgeshire, UK **2021**, pp. 1–48.
[8] F. Zahid, Y. Ke, D. Gall, H. Guo, *Phys. Rev. B* **2010**, *81*, 045406.
[9] K. Huet, in *Laser Annealing Processes in Semiconductor Technology* (Eds: F. Cristiano, A. La Magna), Woodhead Publishing, Burlingame, CA **2021**, pp. 137–173.
[10] K. Huet, J. Aubin, P.-E. Raynal, B. Curvers, A. Verstraete, B. Lespinasse, F. Mazzamuto, A. Sciuto, S. F. Lombardo, A. La Magna, P. Acosta-Alba, L. Dagault, C. Licitra, J.-M. Hartmann, S. Kerdilès, *Appl. Surf. Sci.* **2020**, *505*, 144470.
[11] Q. Xie, Y.-L. Jiang, J. Musschoot, D. Deduytsche, C. Detavernier, R. L. Van Meirhaeghe, S. Van den Berghe, G.-P. Ru, B.-Z. Li, X.-P. Qu, *Thin Solid Films* **2009**, *517*, 4689.
[12] A. Rogozhin, A. Miakonkikh, E. Smirnova, A. Lomov, S. Simakin, K. Rudenko, *Coatings* **2021**, *11*, 117.
[13] O.-K. Kwon, S.-H. Kwon, H.-S. Park, S.-W. Kang, *Electrochem. Solid-State Lett.* **2004**, *7*, C46.
[14] F. Liu, R. Kirchheim, *Scr. Mater.* **2004**, *51*, 521.
[15] S. Simões, R. Calinas, M. T. Vieira, M. F. Vieira, P. J. Ferreira, *Nanotechnology* **2010**, *21*, 145701.
[16] J. M. Ziman, J. M. Ziman, in *Electrons and Phonons: The Theory of Transport Phenomena in Solids*, Oxford University Press, Oxford, New York **2001**.
[17] W. Zhang, S. H. Brongersma, Z. Li, D. Li, O. Richard, K. Maex, *J. Appl. Phys.* **2007**, *101*, 063703.
[18] P. M. Th, M. van Attekum, P. H. Woerlee, G. C. Verkade, A. A. M. Hoeben, *Phys. Rev. B* **1984**, *29*, 645.
[19] G. Kästle, H.-G. Boyen, A. Schröder, A. Plettl, P. Ziemann, *Phys. Rev. B* **2004**, *70*, 165414.
[20] A. Bid, A. Bora, A. K. Raychaudhuri, *Phys. Rev. B* **2006**, *74*, 035426.
[21] G. D. Marzi, D. Iacopino, A. J. Quinn, G. Redmond, *J. Appl. Phys.* **2004**, *96*, 3458.
[22] R. R. Rao, J. V. S. S. N. Murthy, *Zeitschrift für Naturforschung A* **1979**, *34*, 724.
[23] R. Ramji Rao, A. Ramanand, *J. Low Temp. Phys.* **1977**, *27*, 837.
[24] Y. Petrov, K. Migdal, N. Inogamov, V. Khokhlov, D. Ilnitsky, I. Milov, N. Medvedev, V. Lipp, V. Zhakhovsky, *Data Brief* **2020**, *28*, 104980.
[25] S. S. Ezzat, P. D. Mani, A. Khaniya, W. Kaden, D. Gall, K. Barmak, K. R. Coffey, *J. Vac. Sci. Technol. A* **2019**, *37*, 031516.
[26] T. Zhou, D. Gall, *Phys. Rev. B* **2018**, *97*, 165406.
[27] E. Milosevic, S. Kerdsongpanya, A. Zangiabadi, K. Barmak, K. R. Coffey, D. Gall, *J. Appl. Phys.* **2018**, *124*, 165105.
[28] D. Gall, *J. Appl. Phys.* **2020**, *127*, 050901.
[29] S. Kim, H. Suhl, I. K. Schuller, *Phys. Rev. Lett.* **1997**, *78*, 322.
[30] A. F. Mayadas, M. Shatzkes, J. F. Janak, *Appl. Phys. Lett.* **1969**, *14*, 345.
[31] K. Fuchs, *Math. Proc. Cambridge Philos. Soc.* **1938**, *34*, 100.
[32] E. H. Sondheimer, *Adv. Phys.* **1952**, *1*, 1.
[33] T. Sun, B. Yao, A. P. Warren, K. Barmak, M. F. Toney, R. E. Peale, K. R. Coffey, *Phys. Rev. B* **2010**, *81*, 155454.
[34] D. Kojda, R. Mitdank, M. Handwerg, A. Mogilatenko, M. Albrecht, Z. Wang, J. Ruhhammer, M. Kroener, P. Woias, S. F. Fischer, *Phys. Rev. B* **2015**, *91*, 024302.
[35] G. Schwarz, *Ann. Stat.* **1978**, *6*, 461.
[36] C. T. Volinsky, A. E. Raftery, *Biometrics* **2000**, *56*, 256.
[37] A. E. Raftery, *Biometrika* **1996**, *83*, 251.
[38] Y. F. Zhu, X. Y. Lang, W. T. Zheng, Q. Jiang, *ACS Nano* **2010**, *4*, 3781.
[39] I. Karmous, F. Roze, P.-E. Raynal, K. Huet, P. A. Alba, T. Tabata, S. Kerdiles, *ECS Trans.* **2021**, *102*, 125.
[40] I. Karmous, F. Rozé, P.-E. Raynal, K. Huet, P. A. Alba, T. Tabata, S. Kerdilès, *ECS J. Solid State Sci. Technol.* **2022**, *11*, 104006.
[41] Y. F. Lu, W. K. Choi, Y. Aoyagi, A. Kinomura, K. Fujii, *J. Appl. Phys.* **1996**, *80*, 7052.
[42] H. Mei, C. M. Landis, R. Huang, *Mech. Mater.* **2011**, *43*, 627.
[43] H. Chai, C. D. Babcock, W. G. Knauss, *Int. J. Solids Struct.* **1981**, *17*, 1069.
[44] H.-H. Yu, J. W. Hutchinson, *Int. J. Fract.* **2002**, *113*, 39.
[45] J. W. Hutchinson, Z. Suo, in *Advances in Applied Mechanics* (Eds: J. W. Hutchinson, T. Y. Wu), Elsevier, Amsterdam, Netherlands **1991**, pp. 63–191.
[46] Y. Estrin, G. Gottstein, E. Rabkin, L. S. Shvindlerman, *Acta Mater.* **2001**, *49*, 673.
[47] P. Chaudhari, *J. Vac. Sci. Technol.* **1972**, *9*, 520.
[48] R. Daniel, D. Holec, M. Bartosik, J. Keckes, C. Mitterer, *Acta Mater.* **2011**, *59*, 6631.
[49] S. F. Lombardo, S. Boninelli, F. Cristiano, I. Deretzis, M. G. Grimaldi, K. Huet, E. Napolitani, A. La Magna, *J. Appl. Phys.* **2018**, *123*, 105105.
[50] S. F. Lombardo, G. Fisicaro, I. Deretzis, A. La Magna, B. Curver, B. Lespinasse, K. Huet, *Appl. Surf. Sci.* **2019**, *467–468*, 666.
[51] R. Monflier, T. Tabata, H. Rizk, J. Roul, K. Huet, F. Mazzamuto, P. Acosta Alba, S. Kerdilès, S. Boninelli, A. La Magna, E. Scheid, F. Cristiano, E. Bedel-Pereira, *Appl. Surf. Sci.* **2021**, *546*, 149071.

© 2024 The Author(s). Advanced Engineering Materials published by Wiley-VCH GmbH

15272648, 2025, 4, Downloaded from https://advanced.onlinelibrary.wiley.com/doi/10.1002/adem.202402656, Wiley Online Library on [05/02/2026]. See the Terms and Conditions (https://onlinelibrary.wiley.com/terms-and-conditions) on Wiley Online Library for rules of use; OA articles are governed by the applicable Creative Commons License

[52] L. Dagault, P. Acosta-Alba, S. Kerdilès, J. P. Barnes, J. M. Hartmann, P. Gergaud, T. T. Nguyen, A. Grenier, A. M. Papon, N. Bernier, V. Delaye, J. Aubin, F. Cristiano, *ECS J. Solid State Sci. Technol.* **2019**, *8*, P202.
[53] A. P. Baddorf, V. Jahns, D. M. Zehner, H. Zajonz, D. Gibbs, *Surf. Sci.* **2002**, *498*, 74.
[54] J. W. Arblaster, *Platinum Met. Rev.* **2013**, *57*, 127.
[55] X.-G. Lu, M. Selleby, B. Sundman, *Calphad* **2005**, *29*, 68.
[56] B. G. Childs, *Rev. Mod. Phys.* **1953**, *25*, 665.
[57] B. Zhang, X. Li, D. Li, *Calphad* **2013**, *43*, 7.
[58] E. Güler, Ş. Uğur, M. Güler, G. Uğur, *Eur. Phys. J. Plus* **2024**, *139*, 372.
[59] M. Wang, Z. Ye, F. Yang, Y. Chen, T. Gao, J. Wei, F. Gou, *Int. J. Hydrogen Energy* **2024**, *50*, 85.
[60] Z.-L. Liu, C.-C. Zhu, X.-L. Zhang, H.-Y. Wang, *Phys. B* **2020**, *598*, 412434.
[61] B. D. K. Pandey, D. Singh, P. K. Yadawa, *Platinum Met. Rev.* **2009**, *53*, 91.
[62] A. Kozma, *Technol. Transfer: Fundam. Princ. Innovative Tech. Solutions* **2020**, *4*, 14.
[63] E. Mohammadpour, M. Altarawneh, J. Al-Nu'airat, Z.-T. Jiang, N. Mondinos, B. Z. Dlugogorski, *Mol. Simul.* **2018**, *44*, 415.
[64] Z. H. Cen, B. X. Xu, J. F. Hu, R. Ji, Y. T. Toh, K. D. Ye, Y. F. Hu, *J. Phys. D: Appl. Phys.* **2017**, *50*, 075105.
[65] A. Seifitokaldani, A. E. Gheribi, M. Dollé, P. Chartrand, *J. Alloys Compd.* **2016**, *662*, 240.
[66] H. Holleck, *J. Vac. Sci. Technol. A* **1986**, *4*, 2661.
[67] F. I. Ajami, R. K. MacCrone, *J. Less Common Met.* **1974**, *38*, 101.
[68] H. Tada, A. E. Kumpel, R. E. Lathrop, J. B. Slanina, P. Nieva, P. Zavracky, I. N. Miaoulis, P. Y. Wong, *J. Appl. Phys.* **2000**, *87*, 4189.
[69] J.-H. Zhao, T. Ryan, P. S. Ho, A. J. McKerrow, W.-Y. Shih, *J. Appl. Phys.* **1999**, *85*, 6421.
[70] G. Carlotti, L. Doucet, M. Dupeux, *Thin Solid Films* **1997**, *296*, 102.
[71] B. El-Kareh, in *Fundamentals of Semiconductor Processing Technology*, Springer US, Boston, MA **1995**.
[72] J. T. Fitch, G. Lucovsky, E. Kobeda, E. A. Irene, *J. Vac. Sci. Technol. B: Microelectron. Process. Phenom.* **1989**, *7*, 153.
[73] E. Kobeda, E. A. Irene, *J. Vac. Sci. Technol. B: Microelectron. Process. Phenom.* **1986**, *4*, 720.
[74] N. V. Rumak, V. V. Khatko, V. N. Plotnikov, *Phys. Status Solidi* **1984**, *86*, 93.
[75] I. Blech, U. Cohen, *J. Appl. Phys.* **1982**, *53*, 4202.
[76] H. Watanabe, N. Yamada, M. Okaji, *Int. J. Thermophys.* **2004**, *25*, 221.
[77] T. Middelmann, A. Walkov, G. Bartl, R. Schödel, *Phys. Rev. B* **2015**, *92*, 174113.
[78] W. M. Yim, R. J. Paff, *J. Appl. Phys.* **1974**, *45*, 1456.
[79] H. Nejat Pishkenari, E. Mohagheghian, A. Rasouli, *Phys. Lett. A* **2016**, *380*, 4039.
[80] M. Okaji, *Int. J. Thermophys.* **1988**, *9*, 1101.
[81] M. A. Hopcroft, W. D. Nix, T. W. Kenny, *J. Microelectromech. Syst.* **2010**, *19*, 229.
[82] J. J. Wortman, R. A. Evans, *J. Appl. Phys.* **1965**, *36*, 153.
[83] E. J. Boyd, D. Uttamchandani, *J. Microelectromech. Syst.* **2012**, *21*, 243.
[84] C.-H. Cho, *Curr. Appl. Phys.* **2009**, *9*, 538.

© 2024 The Author(s). Advanced Engineering Materials published by Wiley-VCH GmbH

15272648, 2025, 4, Downloaded from https://advanced.onlinelibrary.wiley.com/doi/10.1002/adem.202402656, Wiley Online Library on [05/02/2026]. See the Terms and Conditions (https://onlinelibrary.wiley.com/terms-and-conditions) on Wiley Online Library for rules of use; OA articles are governed by the applicable Creative Commons License